Sensorless Control System for a Single-Phase DC-Excited Flux-Switching Machine With Self-Starting Capability

ZIH-CING YOU AND SHENG-MING YANG, (Life Member, IEEE)

Department of Electrical Engineering, National Taipei University of Technology, Taipei 106344, Taiwan

Corresponding author: Sheng-Ming Yang (smyang@ntut.edu.tw)

ABSTRACT Single-phase dc-excited flux-switching machine (DCFSM) exhibits low manufacturing cost and rugged structure. This type of machine has better efficiency and torque density than single-phase induction machine and universal machine. In addition, single-phase DCFSM can generate lower torque ripple than other types of single-phase machines, e.g. switch reluctance machine and brushless DC machine. These advantages make it suitable for low-cost variable speed applications. However, single-phase DCFSMs requires accurate position feedback from a position sensor to generate smooth torque. The position sensor such as an encoder is not permitted in the low-cost applications due to its high cost. To eliminate the position sensor, this paper presents a novel sensorless control scheme for single-phase DCFSMs. Rotor position is estimated with the position-dependent armature current ripple induced by injecting high-frequency square-wave voltage to the field winding at standstill and low speeds. At medium and high speeds, armature mutual flux linkage is calculated and used to estimate the rotor position. A seamless transition between these two methods is achieve by mixing the calculated position error signals as the input for a single position estimator. The experimental results show that with the proposed scheme, the single-phase DCFSM can accelerate from standstill to the rated speed with 50% load, and to the maximum speed with 25% load, respectively.

INDEX TERMS DC-excited flux switching machine, single-phase machine, sensorless control, flux linkage estimation, high-frequency voltage injection.

I. INTRODUCTION

Single-phase dc-excited flux-switching machines (DCFSMs) have low manufacturing cost due to magnetic field is generated by field windings rather than magnets. The structure of DCFSMs is rugged since the armature and field windings are located in the stator slots. Moreover, literatures have reported that single-phase DCFSMs exhibit higher efficiency [1]–[4] and lower torque ripple [5] than other type of single-phase machine, e.g. single-phase induction machines (IMs), universal machines (UMs), and single-phase brushless dc machine (BLDC).

Similar to the other types of single-phase machines, single-phase DCFSMs also encounter start-up problem as the rotor parks nearby the commutation positions, where the armature current commutates [6]–[9]. To solve this problem, the authors in [10] proposed a two-layer rotor for single-phase

The associate editor coordinating the review of this manuscript and approving it for publication was Paolo Giangrande.

DCFSMs. The two-layer rotor is composed of a standard doubly-salient rotor and an asymmetric pole shoe rotor. With this two-layer rotor, the motor can start-up nearby the commutation positions with the significant reluctance torque produced by the field current.

Another problem of single-phase machines is the amount of the torque ripple. In general, torque ripple of single-phase DCFSMs is greater than 100% because of the commutation of armature current. A torque ripple reduction scheme was presented in [5], and it was implemented on the single-phase DCFSM with a two-layer rotor presented in [10]. This machine exhibits a complementary torque characteristic due to the two-layer rotor structure. On the basis of this unique characteristic, the armature and field current profiles were established to generate smooth torque response and low torque ripple. The experimental results demonstrated that torque ripple can be reduced to approximately 30%, and the speed regulation performance is excellent. However, this control system relies on an accurate position feedback, which

is not permitted because the single-phase DCFSMs usually target for the low-cost applications.

Numerous sensorless control schemes for electric machines were proposed to eliminate the need for physical position sensors over the last two decades. These schemes are generally divided into two categories: (i) model-based (MB), and (ii) high-frequency-voltage-injection (HFVI). In the MB methods, rotor position is estimated by using a phase-lock loop (PLL) to track the back-electromotive force (EMF) [11]–[13] or the stator flux linkage [14]–[19]. These methods were experimentally validated that they can provide satisfactory performance at medium and high speeds. In contrast to the MB methods, a high-frequency (HF) voltage signal is injected into the machine for HFVI methods. Then, the position-dependent current component is demodulated from the difference of HF current and used to estimate rotor position [20]–[23]. In general, HFVI method provides better performance at standstill and low speeds.

Majority of the aforementioned studies are focused on three-phase machines. Sensorless control for single-phase machines are rarely discussed. The authors in [24]–[27] presented a method to estimate rotor position of single-phase brushless dc ma-chines (BLDCs) and single-phase IMs by tracking the stator flux on the virtual rotor-reference frame, taking the advantage of the phase-split capacitor and the starting winding. In [28], [29], the zero-crossing points (ZCPs) of the machine's back-EMF were detected and used to commutate armature current. However, the machine's capability of start-up with a heavy load was not demonstrated.

This paper presents a novel sensorless control scheme for single-phase DCFSMs. Rotor position is estimated with the difference of HF armature current by injecting a HF square-wave voltage into the field winding at standstill and low speeds. At medium and high speeds, rotor position is estimated by tracking the armature mutual flux linkage with a novel single-phase PLL. A seamless transition between these two methods is achieved with a single position estimator. The estimated position can successfully integrated into the torque ripple reduction control presented in [5]. In addition, the experiment results demonstrate that with the proposed sensorless control, the machine can start up with a 50% rated load. Therefore, with the proposed sensorless control, the single-phase DCFSM can be a good alternative for low-cost variable speed applications in which the other type of single-phase machines is usually adopted.

This paper is organized into seven sections. An overview about the challenges of sensorless control of the single-phase DCFSM is highlighted in Section I. The studied single-phase DCFSM and the control system is introduced in Section II. In Section III, the sensorless control using the armature mutual flux linkage is formulated. The sensorless control based on the HFVI is presented in Section IV. The starting procedure and the integration of two sensorless controls is presented in Section V. The performance of the proposed control system is demonstrated in Section VI. Finally, conclusions are stated in Section VII.
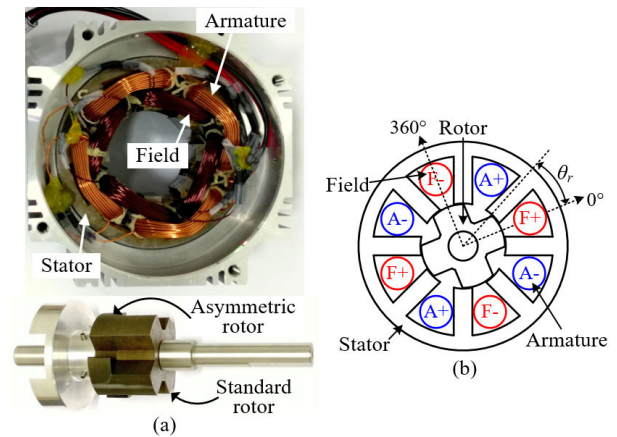
FIGURE 1. (a) Image of studied single-phase DCFSM and (b) cross-sectional view (only standard rotor visible) [10].

II. OVERVIEW OF THE PROPOSED CONTROL SYSTEM

The machine studied in this paper is an eight-slot, four-pole, single-phase DCFSM with a two-layer rotor. Its rotor is composed of a standard doubly-salient rotor and an asymmetric pole shoe rotor, as shown in Fig. 1(a) [10]. Fig. 1(b) displays the cross-sectional view of the machine to show the winding configuration, where θ_r denotes the rotor electrical position. For a clear observation, only the doubly-salient rotor is shown in this figure. The main parameters of the machine are listed in Table 1, Appendix.

According to the energy conversion principle, the generated torque is expressed as follows:

$$T_e = P\left[\frac{i_a^2}{2}\frac{d}{d\theta_r}L_{as} + \frac{i_f^2}{2}\frac{d}{d\theta_r}L_{fs} + i_a\frac{d}{d\theta_r}\left(i_f L_m\right)\right]$$
$$= T_{relucA} + T_{relucF} + T_m, \qquad (1)$$

where P is the number of rotor poles; i_a and i_f are the armature and field currents, respectively; L_{as} and L_{fs} are the armature and field self-inductances, respectively; and L_m is the mutual inductance. The generated torque comprises three components: (i) the electromagnetic torque generated by both currents and the mutual inductance (T_m); (ii) the reluctance torque generated by the armature current and its self-inductance (T_{relucA}); and (iii) the reluctance torque generated by the field current and its self-inductance (T_{relucF}). Fig. 2 presents the calculated self-inductances and mutual inductance.
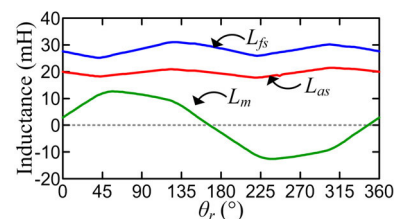

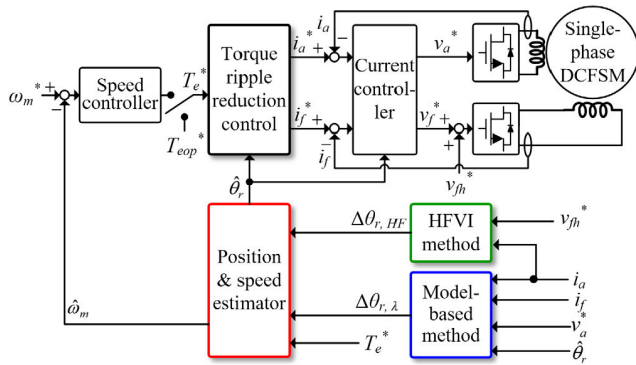**FIGURE 2.** Calculated self-inductances and mutual inductance.

FIGURE 3. Schematic of proposed sensorless control system.

Fig. 3 illustrates the proposed sensorless control system, with *, ^, and ω_m denoting the command, estimated value, and shaft speed, respectively. The control system comprised four components: the (i) speed controller; (ii) torque ripple reduction controller; (iii) current controller; and (iv) rotor position and speed estimator. A simple proportional-plus-integral regulator was used for speed control. This study adopted the torque ripple reduction scheme and current controller presented in [5]. These controllers require rotor position information to generate current commands and, in turn, control the currents. In general, this paper reports on a scheme for estimating the position and speed of a rotor; this scheme also integrates the estimated position, estimated speed into the controllers for the sensorless control.
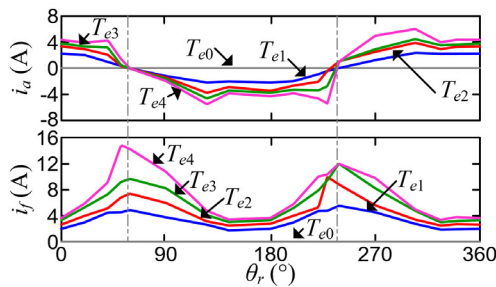

FIGURE 4. Current commands for different torque values [5].

The torque ripple reduction scheme employs the studied machine's complementary torque characteristic to generate current command profiles. The current commands for various torque values are displayed in Fig. 4, where T_{e0}, T_{e1}, T_{e2}, T_{e3}, and T_{e4} denote 0%, 25%, 50%, 75%, and 100% of the rated torque, respectively. The measured torque waveforms are presented in Fig. 5. The armature current commutation positions marked by the gray dashed line indicate that the significant reluctance torque (T_{relucF}) is produced by the field current to compensate for the loss of T_m and to suppress the torque ripple. With the assistance of T_{relucF}, the machine can start up at any position.

As presented in Fig. 3, rotor position is estimated with the HFVI method at standstill and low speeds. A HF square-wave
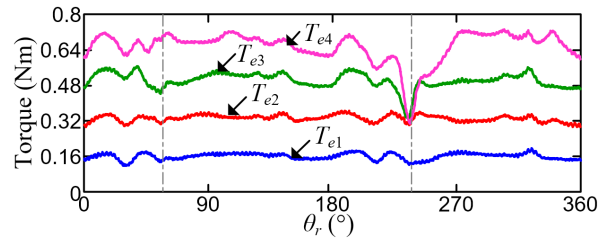

FIGURE 5. Motor torque measured with the current commands presented in Fig. 4 [5].

voltage signal (v_{fh}^*) is injected into the field winding, the position-dependent current ripple in the armature winding is measured, and its difference is calculated. Subsequently, a position identifier is proposed to estimate the rotor position with the calculated current. At medium and high speeds, rotor position is estimated using the MB method. The mutual flux linkage induced on the armature winding is estimated using a closed-loop flux estimator, and the rotor position is estimated through tracking the flux linkage with a novel single-phase PLL. During the transitional region the position error signals calculated with the HFVI and MB methods are mixed with a speed-dependent weighting function, and then inputted for a position estimator. The following sections in this paper describe the position estimation schemes.

III. POSITION ESTIMATION WITH MODEL-BASED METHOD

Armature winding voltage (v_a) and field winding voltage (v_f) are expressed as follows:

$$v_a = i_a r_a + s(i_a L_{as}) + s(i_f L_m)$$
$$v_f = i_f r_f + s(i_f L_{fs}) + s(i_a L_m), \quad (2)$$

where s is the Laplace operator; r_a and r_f are the armature and field winding resistances, respectively; and ω_r is the electrical speed. Because mutual inductance is position-dependent, the induced back-EMF can be used to estimate rotor position. However, because this back-EMF is sensitive to the pulsating field current, the mutual flux linkage (λ_{am}) produced by the field current is used for rotor position estimation instead.

A. MUTUAL FLUX ESTIMATOR
The armature flux linkage (λ_{as}) can be calculated with either the voltage model from (2), denoted as

$$\lambda_{as} = (v_a - i_a r_a)/s \quad (3)$$

or with the current model from (2)

$$\lambda_{as} = (i_a L_{as}) + (i_f L_m). \quad (4)$$

According to (4), λ_{am} is expressed as follows.

$$\lambda_{am} = \lambda_{as} - (i_a L_{as}) = i_f L_m \quad (5)$$

Subsequently, the armature current can be estimated from the estimated flux linkage with estimated parameters as

follows.

$$\hat{i}_a = \left(\hat{\lambda}_{as} - i_f \hat{L}_m\right) \Big/ \hat{L}_{as} \quad (6)$$

Because the flux linkage calculated with (3) is highly sensitive to the armature voltage offset and drift [14]–[15],[17], a closed-loop estimator was developed to estimate flux linkage through the convergence of the estimated armature current to the actual current [18]–[19].
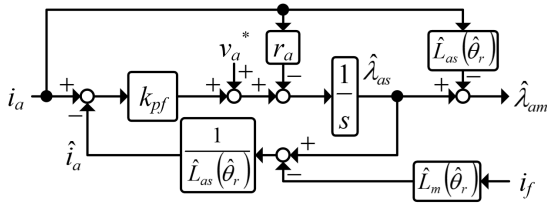

FIGURE 6. Mutual flux estimator.

Fig. 6 illustrates the proposed mutual flux estimator. The inductances (L_{as} and L_m) are functions of rotor position, pre-measured and stored in the controller's lookup tables. Armature flux linkage is first evaluated using the voltage model in (3) and the voltage command. Subsequently, armature current is estimated with (6); the error between the measured and the estimated armature current is regulated by the proportional control (with the gain k_{pf}) to suppress the offset and drift on the estimated flux linkage. Finally, mutual flux linkage is calculated with the estimated flux linkage ($\hat{\lambda}_{as}$) as follows.

$$\hat{\lambda}_{am} = \hat{\lambda}_{as} - \left(i_a \hat{L}_{as}\right) \quad (7)$$

In this study, the acceptable estimation performance is achieved through the experimental tuning of k_{pf} to 1.

From Fig. 6, $\hat{\lambda}_{as}$ can be derived as follows.

$$\left(i_a - \hat{i}_a\right) \cdot k_{pf} + \left(v_a^* - i_a r_a\right) = s \cdot \hat{\lambda}_{as} \quad (8)$$

Substituting (3), (4), and (6) into (8), $\hat{\lambda}_{as}$ is derived as

$$\hat{\lambda}_{as} = \frac{\left(k_{pf}/L_{as}\right)}{s + k_{pf}\big/\hat{L}_{as}} \cdot \hat{\lambda}_{as,I} + \frac{s}{s + k_{pf}\big/\hat{L}_{as}} \cdot \hat{\lambda}_{as,V}$$
$$- \frac{k_{pf}\left(L_m \hat{L}_{as} - \hat{L}_m L_{as}\right)}{L_{as}\hat{L}_{as}\left(s + k_{pf}\big/L_{as}\right)} \cdot i_f, \quad (9)$$

where $\lambda_{as,I}$ and $\lambda_{as,V}$ are the flux linkages calculated from the current and voltage models, respectively. At low frequencies, $\lambda_{as,I}$ dominates. In addition, the offset and drift on $\lambda_{as,V}$ can be suppressed with the high-pass filter established by the proportional controller to eliminate integral windup. Furthermore, assuming $\lambda_{as,I} \approx \lambda_{as,V} = \lambda_{as}$, $\hat{\lambda}_{as}$ can be approximated as follows.

$$\hat{\lambda}_{as} = \frac{s + k_p/L_{as}}{s + k_p\big/\hat{L}_{as}}\lambda_{as} - \frac{k_p\left(L_m \hat{L}_{as} - \hat{L}_m L_{as}\right)}{L_{as}\hat{L}_{as}\left(s + k_p\big/\hat{L}_{as}\right)}i_f \quad (10)$$

Consequently, $\hat{\lambda}_{am}$ can be rewritten as

$$\hat{\lambda}_{am} = \frac{(1-\alpha)\,s}{s + k_{pf}\big/\hat{L}_{as}} \cdot \lambda_{as} + \frac{\alpha \cdot s + k_{pf} \cdot \beta\big/\hat{L}_{as}}{s + k_{pf}\big/\hat{L}_{as}} \cdot \hat{\lambda}_{am}, \quad (11)$$

where $\alpha = \hat{L}_{as}\big/L_{as}$; $\beta = \hat{L}_m\big/L_m$. Equation (11) reveals that $\hat{\lambda}_{am} = \lambda_{am}$ when the inductances are correct.

B. INDUCTANCE COMPENSATION

The inductances of the studied machine are greatly affected by motor torque because of magnetic saturation. As presented in (11), the mismatched inductances result in amplitude and phase distortion of the estimated flux linkage. The estimated flux linkage is distorted at high frequencies due to the mismatch of L_{as} and the differential operation. However, the mismatched L_m disturbs the estimated flux linkage only at low frequencies. In addition, because k_{pf} is the numerator of the second term on the right side of (11), increasing k_{pf} to enhance performance can amplify the effect of inductance mismatch. To compensate for this, the inductances in the flux estimator are adaptively tuned according to the torque command. The relationship between the inductances and torque command were measured experimentally and depicted in Fig. 7. The inductances shown in Fig. 2 were used as the initial values and denoted by a subscripted 0. Both inductances decrease at high torque commands; at low torque commands, however, the inductances are slightly less than the initial values because of the FEM model error.
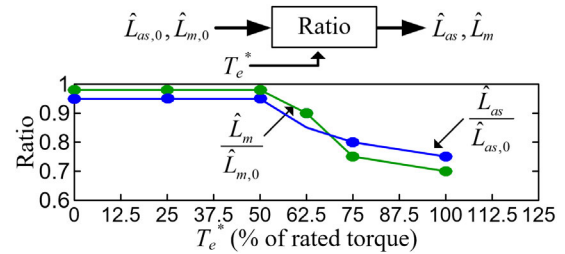

FIGURE 7. Compensation of inductances in the flux estimator.

C. ROTOR POSITION ESTIMATION

Fig. 8(a) presents the λ_{am} waveform calculated with the inductances described in Fig. 2 and with $T_e^* = T_{e1}$. λ_{am} is similarly sinusoidal. A general form for λ_{am} can be established as

$$\lambda_{am} = \lambda_{am,1} \sin\left(\theta_r + \varphi_1\right) + \sum_k \lambda_{am,k} \sin\left(k\theta_r + \varphi_k\right), \quad (12)$$

where the subscripted 1 denotes the fundamental component; ϕ is the phase shift; and k is a positive integer denoting the order of the harmonic. The use of PLL to estimate the position of a single-phase signal has been widely discussed in [30]–[34]. The input signal is first multiplied by a sine or cosine function, and the result is processed with a low-pass

filter (LPF). After the harmonics are filtered, a low-frequency component is obtained that is relevant to the position error between the input signal and the trigonometric function. Finally, an estimator is used, converging the phase error to zero to estimate the position. However, this type of PLL cannot estimate the position effectively when the frequency varies significantly, and the estimator performance is highly dependent on the amplitude of the input signal.
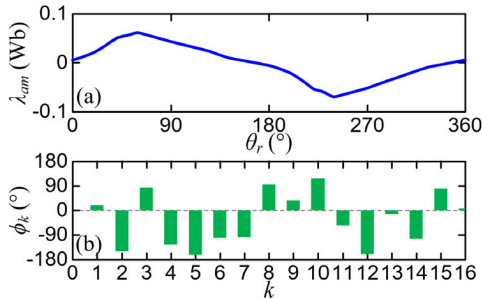

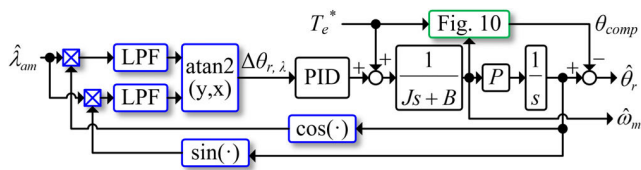**FIGURE 8.** Waveform of calculated (a) λ_{am} and (b) ϕ_k.

FIGURE 9. Proposed position estimator for model-based method.

The proposed single-phase PLL is depicted in Fig. 9, where J is the combined inertia of the rotor and load, and B is the friction coefficient. The input signal is multiplied by a sine and a cosine function, and the results are as follows.

$$
\begin{aligned}
\hat{\lambda}_{am} \sin \hat{\theta}_r &\\
= \frac{\hat{\lambda}_{am,1}}{2} &\left(\cos \left(\theta_r + \varphi_1 - \hat{\theta}_r \right) - \cos \left(\theta_r + \varphi_1 + \hat{\theta}_r \right) \right) \\
&+ \sum_k \hat{\lambda}_{am,k} \sin \left(k\theta_r + \varphi_k \right) \cdot \sin \hat{\theta}_r
\end{aligned} \tag{13}
$$

$$
\begin{aligned}
\hat{\lambda}_{am} \cos \hat{\theta}_r &\\
= \frac{\hat{\lambda}_{am,1}}{2} &\left(\sin \left(\theta_r + \varphi_1 + \hat{\theta}_r \right) + \sin \left(\theta_r + \varphi_1 - \hat{\theta}_r \right) \right) \\
&+ \sum_k \hat{\lambda}_{am,k} \cos \left(k\theta_r + \varphi_k \right) \cdot \cos \hat{\theta}_r
\end{aligned} \tag{14}
$$

After the harmonics are suppressed with the LPFs, their position error $\Delta\theta_{r,\lambda}$ is calculated with the following four-quadrant inverse tangent function (ATAN2):

$$
\begin{aligned}
&\Delta\theta_{r,\lambda} \\
&= \text{ATAN2} \left(\text{LPF} \left\{ \hat{\lambda}_{am} \cos \hat{\theta}_r \right\}, \text{LPF} \left\{ \hat{\lambda}_{am} \sin \hat{\theta}_r \right\} \right) \\
&= \tan^{-1} \left(\frac{\frac{\omega_{lpf}}{s+\omega_{lpf}} \cdot 0.5 \cdot \hat{\lambda}_{am,1} \sin \left(\theta_r + \varphi_1 - \hat{\theta}_r \right)}{\frac{\omega_{lpf}}{s+\omega_{lpf}} \cdot 0.5 \cdot \hat{\lambda}_{am,1} \cos \left(\theta_r + \varphi_1 - \hat{\theta}_r \right)} \right), \tag{15}
\end{aligned}
$$

where ω_{lpf} denotes the cut-off frequency of the LPFs. When $\theta_r + \varphi_1 - \hat{\theta}_r \approx 0$, (15) can be approximated as follows:

$$
\begin{aligned}
\Delta\theta_{r,\lambda} &\approx \tan^{-1} \left(\frac{\frac{\omega_{lpf}}{s+\omega_{lpf}} \cdot \left(\theta_r + \varphi_1 - \hat{\theta}_r \right)}{\frac{\omega_{lpf}}{s+\omega_{lpf}} \cdot 1} \right) \\
&\approx \frac{\omega_{lpf}}{s + \omega_{lpf}} \cdot \left(\theta_r + \varphi_1 - \hat{\theta}_r \right). \tag{16}
\end{aligned}
$$

The calculation of ATAN2 reduces the influence of the LPFs and normalizes the position error signal by eliminating $\hat{\lambda}_{am,1}$. Consequently, the dynamic response of the estimated position and speed improved.

Subsequently, a zero-phase lag estimator estimates the rotor position by regulating the phase error to zero [12], and a proportional-integral-derivative regulator is used for the estimator. In this paper, the cutoff frequency of the LPFs was set to 50 Hz to provide sufficient bandwidth for speed control. Therefore, the double frequency components can be effectively suppressed when the MB method is implemented. Considering the phase delay introduced by the LPFs, the estimator bandwidth is tuned to 40 Hz to ensure operational stability.

The phase shift of the fundamental component in Fig. 8(b) indicates that λ_{am} marginally leads the rotor position, which causes the estimated position to lead the actual position. Subsequently, armature current will commutate earlier due to the phase lead. Early armature commutation may disturb the motor's back EMF and cause control system instability [35]. To alleviate this problem, a compensation angle (θ_{comp}) as a function of both torque and speed was introduced, as described in Fig. 9; however, speed dependency is negligible in the estimator. Therefore, θ_{comp} was experimentally tuned offline to minimize the error between the torque command and the average torque. The waveform of θ_{comp} is depicted in Fig. 10.
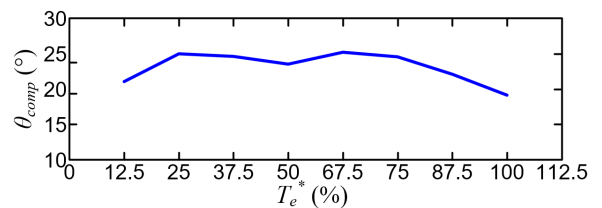

FIGURE 10. Compensation angle versus torque command.

IV. POSITION ESTIMATION WITH HIGH-FREQUENCY VOLTAGE INJECTION METHOD

At low and zero speeds, the proposed MB method must extract the phase error signal with considerably smaller ω_{lpf}. Thus, the system bandwidth deteriorates, rendering it impossible to perform sensorless control. Therefore, a HFVI method with a position identifier was formulated to estimate the rotor position at low and zero speed.

A. HIGH-FREQUENCY MODEL
The HF voltage model can be derived from (2) by ignoring the resistive drop, which is represented as

follows:

$$\begin{bmatrix} v_{ah} \\ v_{fh} \end{bmatrix} = \begin{bmatrix} L_{as} & L_m \\ L_m & L_{fs} \end{bmatrix} s \begin{bmatrix} i_{ah} \\ i_{fh} \end{bmatrix}, \tag{17}$$

where the subscripted h denotes the HF component. Because the inductances fluctuate slowly with the rotor position, the voltage drop caused by the HF currents dominates, whereby (17) can be rewritten as follows:

$$\begin{bmatrix} v_{ah} \\ v_{fh} \end{bmatrix} = \begin{bmatrix} L_{as} & L_m \\ L_m & L_{fs} \end{bmatrix} \frac{\Delta}{\Delta T} \begin{bmatrix} i_{ah} \\ i_{fh} \end{bmatrix}, \tag{18}$$

where Δ is the difference operator and ΔT is the half period of v_{fh}.

To obtain optimal estimation performance, the HF voltage is injected into the field winding, and the position is estimated from the HF armature current [36]. A HF square-wave voltage with amplitude V_h is injected into the field winding and written as follows.

$$\begin{bmatrix} v_{ah} \\ v_{fh} \end{bmatrix} = \begin{bmatrix} 0 \\ \pm V_h \end{bmatrix} \tag{19}$$

The induced HF currents are as follows.

$$\Delta i_{ah} = -\frac{L_m}{L_{as}} \cdot \Delta i_{fh} \tag{20}$$

$$\Delta i_{fh} = \frac{\pm V_h \cdot \Delta T}{L_{fs} - L_m^2/L_{as}} \tag{21}$$

By substituting (21) into (20), the difference of HF armature current can be derived as follows.

$$\Delta i_{ah} = -\frac{L_m}{L_{as}} \cdot \frac{\pm V_h \cdot \Delta T}{L_{fs} - L_m^2/L_{as}} \tag{22}$$

Subsequently, Δi_{ah} is adjusted according to the voltage polarity as follows.

$$\Delta i_{ah} = \begin{cases} \Delta i_{ah}, & v_{fh} > 0 \\ -\Delta i_{ah}, & v_{fh} < 0 \end{cases} \tag{23}$$
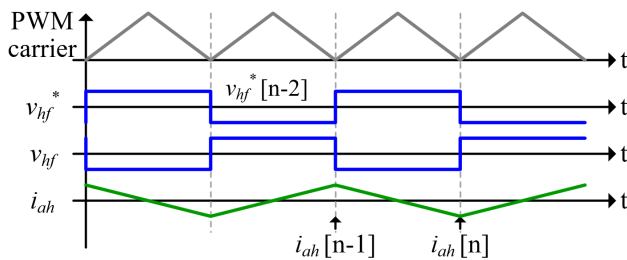

FIGURE 11. Exemplary timing sequence of v_{fh} and i_{ah}.

Fig. 11 illustrates an exemplary timing sequence of v_{fh} and i_{ah}, where the injection voltage changes its polarity, and i_{ah} is sampled at every pulse width modulation (PWM) cycle. With $i_{ah}[n]$ and $i_{ah}[n-1]$ as the present and previous sampled currents, Δi_{ah} is the calculated difference between them. Because of the delay introduced by the PWM, the actual voltage lags the voltage command by one PWM period

(i.e. $i_{ah}[n]$ is induced by the voltage command two PWM periods before). Consequently, the calculation of Δi_{ah} is modified as follows:

$$\Delta i_{ah} = \begin{cases} \Delta i_{ah}, & v_{fh}^*[n-2] > 0 \\ -\Delta i_{ah}, & v_{fh}^*[n-2] < 0 \end{cases} \tag{24}$$

B. ROTOR POSITION ESTIMATION

The difference of current calculated with the inductances in Fig. 2 is represented in Fig. 12(a), where $V_h = 78$ V and $\Delta T = 1/16000$ for example. Δi_{ah} is a single-phase signal fluctuating one cycle per electrical period. Because the LPFs become ineffective at low speeds, the position estimator presented in Fig. 8 is unsuitable for Δi_{ah}. Instead, a position identifier is proposed to detect discrete rotor positions with Δi_{ah}, where a position estimator is then employed to smooth the discrete rotor position.
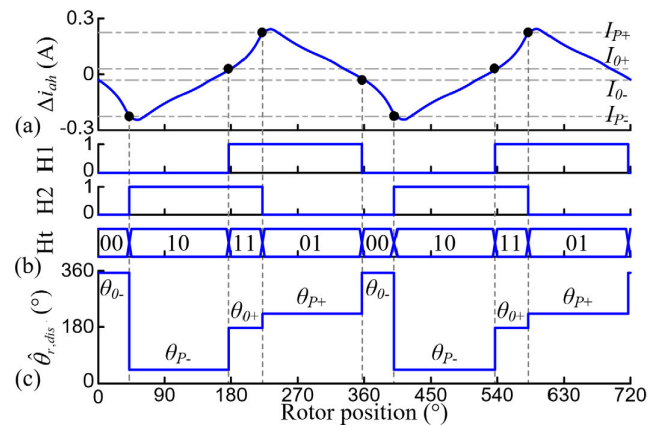

FIGURE 12. Waveforms of (a) calculated Δi_{ah}; (b) signals H1, H2, and Ht; and (c) estimated discrete position.
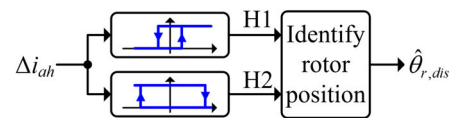

FIGURE 13. Position identifier.

Fig. 13 illustrates the position identifier, and the waveforms depicted in Fig. 12(b) and (c) explain its operations. Two hysteresis comparators detect the status of Δi_{ah}. One comparator with the thresholds of I_{0+} and I_{0-} detects the ZCPs of Δi_{ah}, and its output is denoted by H1. H1 becomes high level when $\Delta i_{ah} > I_{0+}$, and it becomes low level when $\Delta i_{ah} < I_{0-}$. Another comparator with the thresholds of I_{P+} and I_{P-} detects the maximum and minimum of Δi_{ah}, and its output is denoted by H2. H2 becomes low level when $\Delta i_{ah} > I_{P+}$, and it becomes high level when $\Delta i_{ah} < I_{P-}$. H1 and H2 are then combined and denoted by Ht. Four rotor positions are identified within one electrical period according to the levels of Ht. They are marked as $\theta_{P-}, \theta_{0+}, \theta_{P+},$ and θ_{0-}, with the discrete rotor position denoted as $\hat{\theta}_{r,dis}$.

Because the resolution of $\hat{\theta}_{r,dis}$ is low, a zero-phase lag estimator is used to process a smooth position estimation. Fig. 14 presents the block diagram of the estimator, where $\Delta\theta_{r,HF}$ is the position error. The estimator bandwidth is tuned to 25 Hz to suppress the HF harmonics on $\hat{\theta}_{r,dis}$ and to retain sufficient bandwidth for speed control.
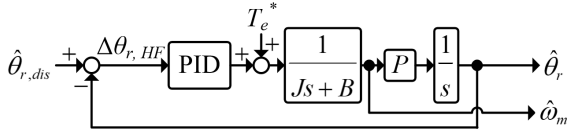

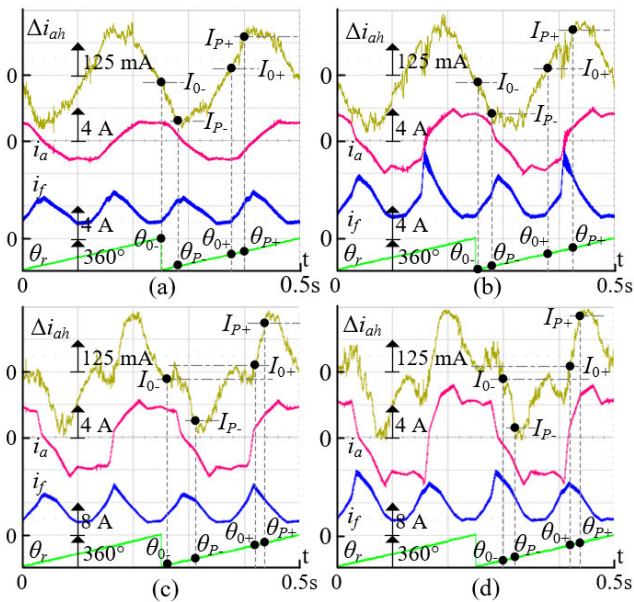**FIGURE 14.** Position identifier for the HFVI method.

FIGURE 15. Δi_{ah} measured at torque ratings of T_e^* = (a) 25%, (b) 50%, (c) 75%, and (d) 100%.

C. SETTING OF POSITION IDENTIFIER

Because Δi_{ah} is greatly affected by magnetic saturation, the thresholds and values of $\hat{\theta}_{r,dis}$ at different Ht levels are tuned experimentally. Fig. 15 presents Δi_{ah} measured at different torque commands. The frequency of the injection voltage is set to 8 kHz (half of PWM frequency) to avoid HF current disturbing the current controller. In addition, the magnitude of the injection voltage is set to 78 V because Δi_{ah} can have lowest total harmonic distortion (THD) and ensure sufficient signal-to-noise ratio (SNR). When T_e^* > 75% (Fig. 15(c) and (d)), the ZCPs of Δi_{ah} are distorted so that the machine cannot generate sufficient torque at θ_{0+} and θ_{0-}. Therefore, the HFVI method is not feasible for torque rated at T_e^* > 75%. Still effective for torque rated at T_e^* < 65%, the maximum torque command for the HFVI method (T_e^* = 65%) is denoted by T_{eop}^* in the experimental verifications. Table 2 lists the thresholds settings and values of $\hat{\theta}_{r,dis}$ for various torque commands.
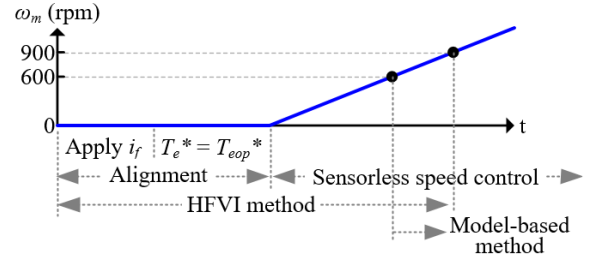

FIGURE 16. Starting procedures of sensorless control system.

V. INTEGRATION OF MODEL-BASED AND HFVI SCHEMES

Fig. 16 illustrates the starting procedures for the sensorless control system. Prior to speed control activation, an alignment is performed to move the rotor to a nonzero torque position by the reluctance torque with the application of i_f. For single-phase DCFSMs, initial position cannot be estimated precisely, because rotor positions can correspond to the same level of Δi_{ah}. However, because the studied DCFSM has two nonzero torque positions (i.e., 130° and 304° [10]), after the alignment, the HFVI method is used to identify the exact rotor position according to the polarity of Δi_{ah}. The estimated position $\hat{\theta}_r$ is set to 130° for Δi_{ah} < 0 and set to 304° for Δi_{ah} > 0. It is noted that the machine is suitable for the applications that allows the initial rotor movement due to the alignment procedure. Because a smooth speed control nearby zero speed is difficult to achieve due to the stepwise $\hat{\theta}_{r,dis}$, after the alignment, torque command is set to T_{eop}^* (65% rated torque) to hold the rotor position regardless of the load until the speed controller is activated. On these settings, the machine can start from standstill with any load smaller than T_{eop}^*.

In the speed control mode, speed is controlled with the HFVI and MB methods when the speed is below 600 and above 900 rpm, respectively. Although these two sensorless methods calculate the position error through different approaches, the position estimators are identical. Therefore, between 600 and 900 rpm, the calculated position errors (i.e., $\Delta\theta_{r,\lambda}$ and $\Delta\theta_{r,HF}$) are combined with a speed-dependent weighting function (G_w). Fig. 17 represents the position estimator, and Fig. 18 depicts the waveform of G_w, with a piecewise linear function used for convenience. In addition, the estimator bandwidth is adaptively tuned from 25 to 40 Hz according to $\hat{\omega}_m$ for optimal dynamic response.
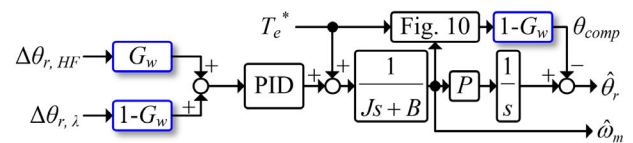

FIGURE 17. Position estimator with mixed position errors.

It is noted that the position estimator in Fig. 17 involves the mechanical parameters. The effect on the position estimator causing by the parameter uncertainties was investigated
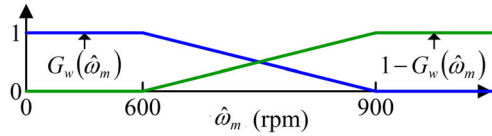
FIGURE 18. Weighting function used in position estimator.

in [12]. The results demonstrated that this type of position estimator is robust against the parameter uncertainties within the estimator bandwidth. In addition, the target applications of single-phase DCFSMs generally require slow dynamic response. Therefore, the parameter uncertainties is a slight issue to the proposed sensroless control. For the applications requiring higher dynamic response, an auto-tuning scheme of mechanical parameters can be integrated to the proposed sensorless control to improve the robustness of the position estimator.
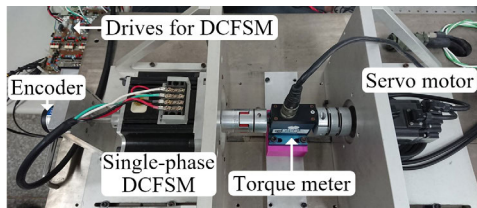

FIGURE 19. Experimental setup.

VI. EXPERIMENTAL RESULTS

Fig. 19 depicts the experimental setup. The studied machine was coupled with a servomotor to provide load torque. An encoder with 2000 pulses per revolution was implemented to monitor the position and shaft speed of the machine to validate performance. A torque meter was connected between the two machines to measure shaft torque. The input dc voltage was 156 V. The proposed sensorless control scheme was implemented on a Texas Instrument's digital signal processor, TMS320F28335. The PWM frequency was 16 kHz, which is identical to the sampling frequency for the torque ripple reduction control, current control, and sensorless control. The sampling frequency for speed control was 2 kHz. The current and speed controller bandwidths were tuned to 1.6 kHz and 5 Hz, respectively. The armature voltage and field voltage is generated by a full-bridge inverter, respectively.

A. LOW-SPEED OPERATIONS

Fig. 20 indicates the dynamic responses when the machine was started at θ_r = (a) 21° and (b) 211°, respectively. A field current of 8 A was applied to align the rotor, which successfully moved to a nonzero torque position following the application of i_f. The HFVI method was then employed to identify the angle of this position. In Fig. 20(a), $\hat{\theta}_r$ was 304° because $\Delta i_{ah} > 0$, and in Fig. 20(b), $\hat{\theta}_r$ was 130° because $\Delta i_{ah} < 0$. Then, T_e^* was gradually increased to T_{eop}^* to hold the rotor position. Subsequently, the rotor moved to the
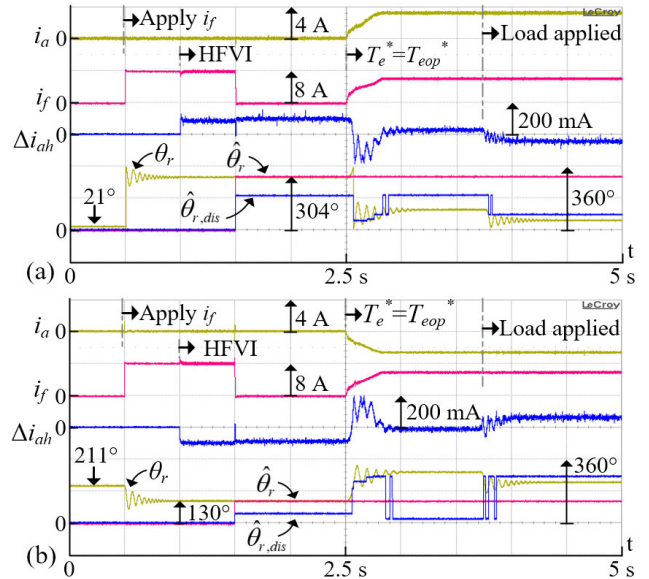

FIGURE 20. Dynamic responses for motor starting at θ_r = (a) 21° and (b) 211°.

commutation position because the external load had yet to be applied. Finally, a 50% load torque was applied, causing the rotor to move slightly to a nearby position. In addition, based on $\hat{\theta}_{r,dis}$ the proposed position identifier was demonstrated to be effective. Because the position estimator had yet to be enabled, $\hat{\theta}_r$ remained unchanged regardless of the load. The position estimator was enabled when the speed control was activated.
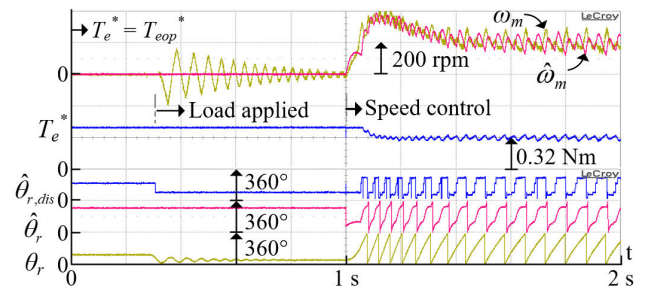

FIGURE 21. Dynamic response when machine accelerated from standstill to 200 rpm with 50% load.

Fig. 21 illustrates the dynamic response when the machine accelerated from standstill to 200 rpm with a 50% load. The rotor was initially held at the commutation position by the torque produced by T_{eop}^*. Following an application of the external load, the rotor oscillated and settled into a new position that was measured using the HFVI method to initialize the position estimator. Subsequently, the machine successfully started with the external load and ran at target speed. As mentioned in Section IV, the external load is limited to a torque rated at 65% to maintain the effectiveness of the HFVI method.

Fig. 22 illustrates the dynamic response when the machine was running at 600 rpm and subjected to a 25% step load.
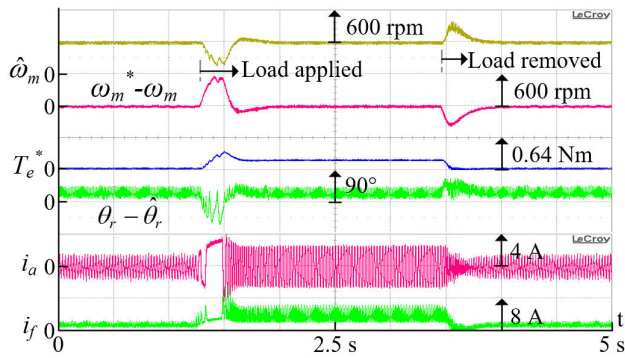
FIGURE 22. Dynamic response when machine was running at 600 rpm and subjected to 25% step load.

The result demonstrates that the shaft speed was successfully controlled at 600 rpm within approximately 0.6 s for both the application and load removal. Even when subjected to a considerable load, with the HFVI method, the machine could start stably and run in the low-speed region.
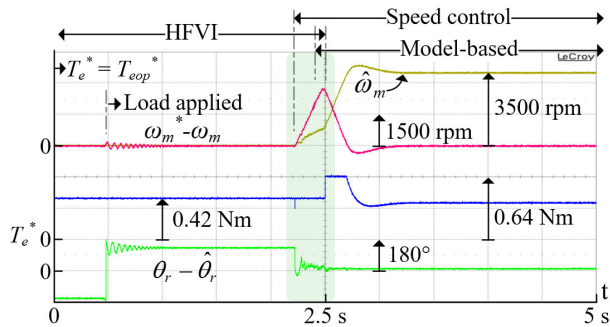

FIGURE 23. Dynamic response when machine accelerated from standstill to 3500 rpm with 50% load.

B. MEDIUM- AND HIGH-SPEED OPERATIONS

Fig. 23 presents the dynamic response when the machine accelerated from standstill to 3500 rpm with a 50% load. Fig. 24 represents the amplified waveforms in the transitional region. The rotor was initially held by T_{eop}^* and, the torque command was also limited to T_{eop}^* for effective HFVI control below 900 rpm. Above 900 rpm, the machine accelerated with 100% of the rated torque because it was controlled with the MB method. Consequently, T_e^* underwent a step change from 0.42 to 0.64 Nm at 900 rpm. Because of the torque limitation, significant speed error was observed during the acceleration period. Nonetheless, the acceleration time was approximately 1 s, and a seamless transition from the HFVI method to the MB method was achieved with the integration of the position errors. Fig. 25 indicates the dynamic response when the machine accelerated from standstill to 6000 rpm with a 25% load. The acceleration time was also approximately 1 s. The results in Fig. 23–25 demonstrate that full-speed operation was achieved through the proposed sensorless control scheme. During the transition, the shaft speed could be smoothly controlled even with considerable torque.
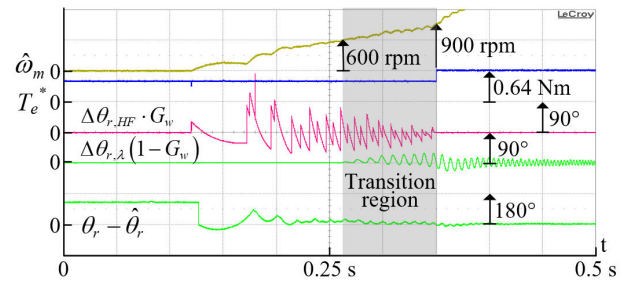

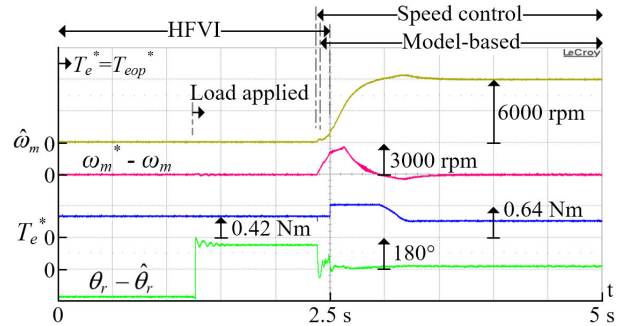**FIGURE 24.** Amplified view of colored area in Fig. 23.

FIGURE 25. Dynamic response when machine accelerated from standstill to 6000 rpm with 25% load.
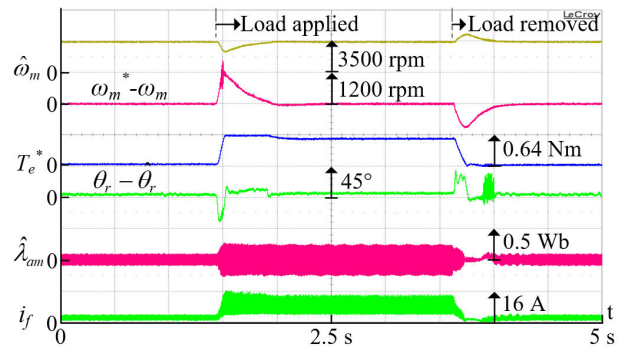

FIGURE 26. Dynamic response when machine was running at 3500 rpm and subjected to 90% step load.
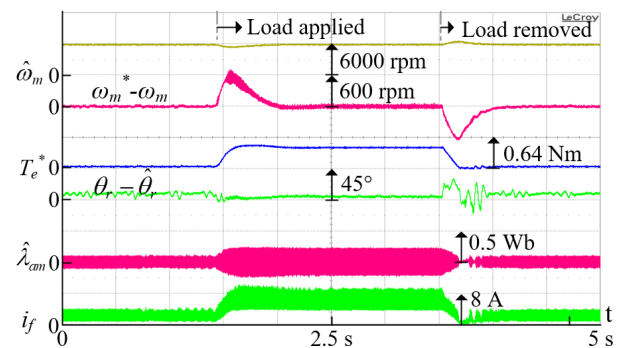

FIGURE 27. Dynamic response when the machine was running at 6000 rpm and subjected to a 40% step load.

Fig. 26–27 describe the dynamic response when the machine was subjected to a 90% step load at 3500 rpm and

to a 40% step load at 6000 rpm, respectively. The shaft speed was successfully controlled to the target speed within 0.7 s for both the load application and load removal. In addition, the proposed flux and rotor position estimators were able to estimate the armature mutual flux linkage and the rotor position under drastic torque change. These results demonstrated that the proposed MB method can provide satisfactory dynamic performance for high-speed operations.

VII. CONCLUSION

This paper presents a novel sensorless control scheme for single-phase DCFSMs. Rotor position was estimated using the HFVI method with a position identifier at standstill and low speeds, and by tracking the armature mutual flux linkage with a single-phase PLL at medium and high speeds. The position error signals calculated with these two methods were mixed with a weighting function during the transitional region. The experimental results demonstrated that the machine can robustly start from standstill provided that the load was smaller than 65% rated torque, accelerated to the rated speed with a 50% load, and accelerated to the maximum speed with a 25% load. Moreover, the machine can effectively recover from a 90% and 40% rated step load change within 1 s while running at constant speed. These results validated the startup and speed regulation performance of the proposed sensorless control system. Consequently, with this control scheme, single-phase DCFSMs can be an alternative for the variable speed applications that usually employ single-phase machines, providing a smooth torque response and robust speed control without the use of positon sensor.

APPENDIX

TABLE 1. Main parameters of single-phase DCFSM.

Parameters	Value	Unit
Stator outer radius	50	mm
Stack length	30	mm
Rated voltage	150	V
Rated speed	3500	rpm
Maximum speed	6000	rpm
Rated torque	0.64	N-m

TABLE 2. Settings of position identifier.

T_e^* (%)	$\hat{\theta}_{r,dis}$ (°)				Threshold (mA)			
	θ_{P-}	θ_{0+}	θ_{P+}	θ_{0-}	I_{P-}	I_{0+}	I_{P+}	I_{0-}
≤ 37.5	51	190	229	16	$-I_{P+}$	20	140	$-I_{0+}$
> 37.5	59	189	255	18	$-I_{P+}$	20	150	$-I_{0+}$
≥ 50	84	192	259	23	$-I_{P+}$	20	160	$-I_{0+}$

REFERENCES

[1] C. Pollock, H. Pollock, and M. Brackley, "Electronically controlled flux switching motors: A comparison with an induction motor driving an axial fan," in *Proc. Ind. Electron. Soc.*, Roanoke, VA, USA, Nov. 2003, pp. 2465–2470, doi: 10.1109/IECON.2003.1280632.

[2] H. Pollock, C. Pollock, R. T. Walter, and B. V. Gorti, "Low cost, high power density, flux switching machines and drives for power tools," in *Proc. 38th IAS Annu. Meeting Conf. Rec. Ind. Appl. Conf.*, Salt Lake City, UT, USA, 2003, pp. 1451–1457, doi: 10.1109/IAS.2003.1257748.

[3] C. Pollock, H. Pollock, R. Barron, J. R. Coles, D. Moule, A. Court, and R. Sutton, "Flux-switching motors for automotive applications," *IEEE Trans. Ind. Appl.*, vol. 42, no. 5, pp. 1177–1184, Sep. 2006, doi: 10.1109/TIA.2006.880842.

[4] J. F. Bangura, "Design of high-power density and relatively high-efficiency flux-switching motor," *IEEE Trans. Energy Convers.*, vol. 21, no. 2, pp. 416–425, Jun. 2006, doi: 10.1109/TEC.2006.874243.

[5] Z.-C. You and S.-M. Yang, "Control system for a single-phase DC-excited flux-switching machine with a torque ripple reduction scheme," *IEEE Access*, vol. 8, pp. 226579–226590, 2020, doi: 10.1109/ACCESS.2020.3045390.

[6] Y. Chen, Y. Chen, Z. Q. Zhu, D. Howe, and Y. Y. Ye, "Starting torque of single-phase flux-switching permanent magnet motors," *IEEE Trans. Magn.*, vol. 42, no. 10, pp. 3416–3418, Oct. 2006, doi: 10.1109/TMAG.2006.879437.

[7] C. L. Chiu, Y. T. Chen, and W. S. Jhang, "Properties of cogging torque, starting torque, and electrical circuits for the single-phase brushless DC motor," *IEEE Trans. Magn.*, vol. 44, no. 10, pp. 2317–2323, Oct. 2008, doi: 10.1109/TMAG.2008.2000761.

[8] M. Fazil and K. R. Rajagopal, "A novel air-gap profile of single-phase permanent-magnet brushless DC motor for starting torque improvement and cogging torque reduction," *IEEE Trans. Magn.*, vol. 46, no. 11, pp. 3928–3932, Nov. 2010, doi: 10.1109/TMAG.2010.2057514.

[9] A.-S. Isfanuti, L. N. Tutelea, I. Boldea, and T. Staudt, "Small-power 4 stator-pole stator-ferrite PMSM single-phase self-starting motor drive: FEM-based optimal design and controlled dynamics," in *Proc. Int. Conf. Optim. Electr. Electron. Equip. (OPTIM)*, Brasov, Romania, May 2017, pp. 517–522, doi: 10.1109/OPTIM.2017.7975020.

[10] Z. C. You, S. M. Yang, C. W. Yu, Y. H. Lee, and S. C. Yang, "Design of a high starting torque single-phase DC-excited flux switching machine," *IEEE Trans. Ind. Electron.*, vol. 64, no. 12, pp. 9905–9913, Dec. 2017, doi: 10.1109/TIE.2017.2696486.

[11] S. Morimoto, K. Kawamoto, M. Sanada, and Y. Takeda, "Sensorless control strategy for salient-pole PMSM based on extended EMF in rotating reference frame," *IEEE Trans. Ind. Appl.*, vol. 38, no. 4, pp. 1054–1061, Jul. 2002, doi: 10.1109/TIA.2002.800777.

[12] H. Kim, M. C. Harke, and R. D. Lorenz, "Sensorless control of interior permanent-magnet machine drives with zero-phase lag position estimation," *IEEE Trans. Ind. Appl.*, vol. 39, no. 6, pp. 1726–1733, Nov./Dec. 2003, doi: 10.1109/TIA.2003.818966.

[13] G.-R. Chen and S.-C. Yang, "Phase voltage measurement for permanent magnet machine sensorless drive using controller capture modulator," *IEEE Trans. Ind. Electron.*, vol. 67, no. 1, pp. 49–58, Jan. 2020, doi: 10.1109/TIE.2019.2896276.

[14] J. Hu and B. Wu, "New integration algorithms for estimating motor flux over a wide speed range," *IEEE Trans. Power Electron.*, vol. 13, no. 5, pp. 969–977, Sep. 1998, doi: 10.1109/63.712323.

[15] J. Holtz and J. Quan, "Drift- and parameter-compensated flux estimator for persistent zero-stator-frequency operation of sensorless-controlled induction motors," *IEEE Trans. Ind. Appl.*, vol. 39, no. 4, pp. 1052–1060, Jul. 2003, doi: 10.1109/TIA.2003.813726.

[16] R. Zhao, Z. Xin, P. C. Loh, and F. Blaabjerg, "A novel flux estimator based on multiple second-order generalized integrators and frequency-locked loop for induction motor drives," *IEEE Trans. Power Electron.*, vol. 32, no. 8, pp. 6286–6296, Aug. 2017, doi: 10.1109/TPEL.2016.2620428.

[17] G.-R. Chen, J.-Y. Chen, and S.-C. Yang, "Implementation issues of flux linkage estimation on permanent magnet machine position sensorless drive at low speed," *IEEE Access*, vol. 7, pp. 164641–164649, 2019, doi: 10.1109/ACCESS.2019.2952371.

[18] Z. Xu and M. F. Rahman, "An adaptive sliding stator flux observer for a direct-torque-controlled IPM synchronous motor drive," *IEEE Trans. Ind. Electron.*, vol. 54, no. 5, pp. 2398–2406, Oct. 2007, doi: 10.1109/TIE.2007.900328.

[19] D. Wang, K. Lu, and P. O. Rasmussen, "Improved closed-loop flux observer based sensorless control against system oscillation for synchronous reluctance machine drives," *IEEE Trans. Power Electron.*, vol. 34, no. 5, pp. 4593–4602, May 2019, doi: 10.1109/TPEL.2018.2865348.

[20] Y.-D. Yoon, S.-K. Sul, S. Morimoto, and K. Ide, "High-bandwidth sensorless algorithm for AC machines based on square-wave-type voltage injection," *IEEE Trans. Ind. Appl.*, vol. 47, no. 3, pp. 1361–1370, May/Jun. 2011, doi: 10.1109/TIA.2011.2126552.

[21] D. Raca, P. Garcia, D. D. Reigosa, F. Briz, and R. D. Lorenz, "Carrier-signal selection for sensorless control of PM synchronous machines at zero and very low speeds," *IEEE Trans. Ind. Appl.*, vol. 46, no. 1, pp. 167–178, Jan. 2010, doi: 10.1109/TIA.2009.2036551.

[22] S.-C. Yang, S.-M. Yang, and J.-H. Hu, "Design consideration on the square-wave voltage injection for sensorless drive of interior permanent-magnet machines," *IEEE Trans. Ind. Appl.*, vol. 64, no. 1, pp. 159–168, Jan. 2017, doi: 10.1109/TIE.2016.2596711.

[23] S. Jung and J.-I. Ha, "Analog filtering method for sensorless AC machine control with carrier-frequency signal injection," *IEEE Trans. Ind. Electron.*, vol. 62, no. 9, pp. 5348–5358, Sep. 2015, doi: 10.1109/TIE.2015.2410257.

[24] L. I. Iepure, I. Boldea, and F. Blaabjerg, "Hybrid I-f starting and observer-based sensorless control of single-phase BLDC-PM motor drives," *IEEE Trans. Ind. Electron.*, vol. 59, no. 9, pp. 3436–3444, Sep. 2012, doi: 10.1109/TIE.2011.2172176.

[25] D.-H. Jang, "Problems incurred in a vector-controlled single-phase induction motor, and a proposal for a vector-controlled two-phase induction motor as a replacement," *IEEE Trans. Power Electron.*, vol. 28, no. 1, pp. 526–536, Jan. 2013, doi: 10.1109/TPEL.2012.2199772.

[26] M. Jemli, H. B. Azza, M. Boussak, and M. Gossa, "Sensorless indirect stator field orientation speed control for single-phase induction motor drive," *IEEE Trans. Power Electron.*, vol. 24, no. 6, pp. 1618–1627, Jun. 2009, doi: 10.1109/TPEL.2009.2014867.

[27] M. N. Almani, G. A. Hussain, and A. A. Zaher, "An improved technique for energy-efficient starting and operating control of single phase induction motors," *IEEE Access*, vol. 9, pp. 12446–12462, 2021, doi: 10.1109/ACCESS.2021.3050920.

[28] Z.-H. Tang, Y.-T. Chen, H.-H. Hsu, R.-H. Liang, and C.-W. Hung, "An initial states recognition (ISR) method for start-up of 1Φ BLDC motor in Hall-sensor-less fan applications," *IEEE Trans. Ind. Electron.*, vol. 67, no. 10, pp. 8302–8311, Oct. 2020, doi: 10.1109/TIE.2019.2947849.

[29] U. Jakobsen, K. Lu, P. O. Rasmussen, D.-H. Lee, and J.-W. Ahn, "Sensorless control of low-cost single-phase hybrid switched reluctance motor drive," *IEEE Trans. Ind. Appl.*, vol. 51, no. 3, pp. 2381–2387, May 2015, doi: 10.1109/TIA.2014.2385939.

[30] R. M. Santos Filho, P. F. Seixas, P. C. Cortizo, L. A. B. Torres, and A. F. Souza, "Comparison of three single-phase PLL algorithms for UPS applications," *IEEE Trans. Ind. Electron.*, vol. 55, no. 8, pp. 2923–2932, Aug. 2008, doi: 10.1109/TIE.2008.924205.

[31] M. Karimi-Ghartemani, "Linear and pseudolinear enhanced phased-locked loop (EPLL) structures," *IEEE Trans. Ind. Electron.*, vol. 61, no. 3, pp. 1464–1474, Mar. 2014, doi: 10.1109/TIE.2013.2261035.

[32] Z. Xin, X. Wang, Z. Qin, M. Lu, P. C. Loh, and F. Blaabjerg, "An improved second-order generalized integrator based quadrature signal generator," *IEEE Trans. Power Electron.*, vol. 31, no. 12, pp. 8068–8073, Dec. 2016, doi: 10.1109/TPEL.2016.2576644.

[33] S. Golestan, J. M. Guerrero, J. C. Vasquez, A. M. Abusorrah, and Y. Al-Turki, "Modeling, tuning, and performance comparison of second-order-generalized-integrator-based FLLs," *IEEE Trans. Power Electron.*, vol. 33, no. 12, pp. 10229–10239, Dec. 2018, doi: 10.1109/TPEL.2018.2808246.

[34] M. N. Ashraf, R. A. Khan, and W. Choi, "A robust PLL technique using a digital lock-in amplifier under the non-sinusoidal grid conditions," in *Proc. 10th Int. Conf. Power Electron.*, Busan, South Korea, May 2019, pp. 2330–2335, doi: 10.23919/ICPE2019-ECCEAsia42246.2019.8797197.

[35] A. Consoli, G. Scelba, G. Scarcella, and M. Cacciato, "An effective energy-saving scalar control for industrial IPMSM drives," *IEEE Trans. Ind. Electron.*, vol. 60, no. 9, pp. 3658–3669, Sep. 2013, doi: 10.1109/TIE.2012.2207651.

[36] H.-Q. Nguyen and S.-M. Yang, "Rotor position sensorless control of wound-field flux-switching machine based on high frequency square-wave voltage injection," *IEEE Access*, vol. 6, pp. 48776–48784, 2018, doi: 10.1109/ACCESS.2018.2867899.

ZIH-CING YOU was born in Taiwan. He received the M.S. degree in electrical engineering from the National Taipei University of Technology, Taipei, Taiwan, in 2017, where he is currently pursuing the Ph.D. degree. His research interests include ac motor drive and control.

SHENG-MING YANG (Life Member, IEEE) was born in Taiwan. He received the M.S. and Ph.D. degrees from the University of Wisconsin–Madison, in 1985 and 1989, respectively. From 1989 to 1992, he was a Development Engineer with Unico Inc., and from 1992 to 1995, he was a Principal Engineer at the Corporate Technology Center, A. O. Smith Company, Milwaukee, WI, USA. In 1995, he joined Tamkang University, Taiwan, as a Professor with the Department of Mechanical and Electro-Mechanical Engineering. Since 2007, he has been with the Department of Electrical Engineering, National Taipei University of Technology, Taiwan. His research interests include ac and dc motor drives and control.

● ● ●